A new contact model for the discrete element method simulation of TiO_2 nanoparticle films under mechanical load

Laube, Jens; Baric, Valentin; Salameh, Samir; Mädler, Lutz; Colombi Ciacchi, Lucio

DOI
10.1007/s10035-018-0799-9

Publication date
2018

Document Version
Final published version

Published in
Granular Matter

Granular Matter (2018) 20:28
https://doi.org/10.1007/s10035-018-0799-9

ORIGINAL PAPER

A new contact model for the discrete element method simulation of TiO_2 nanoparticle films under mechanical load

Jens Laube[1] · Valentin Baric[2] · Samir Salameh[2,3] · Lutz Mädler[2] · Lucio Colombi Ciacchi[1]

Received: 27 September 2017 / Published online: 22 March 2018

Abstract
We develop a novel coarse-grained contact model for Discrete Element Method simulations of TiO_2 nanoparticle films subjected to mechanical stress. All model elements and parameters are derived in a self-consistent and physically sound way from all-atom Molecular Dynamics simulations of interacting particles and surfaces. In particular, the nature of atomic-scale friction and dissipation effects is taken into account by explicit modelling of the surface features and water adsorbate layers that strongly mediate the particle-particle interactions. The quantitative accuracy of the coarse-grained model is validated against all-atom simulations of TiO_2 nanoparticle agglomerates under tensile stress. Moreover, its predictive power is demonstrated with calculations of force-displacement curves of entire nanoparticle films probed with force spectroscopy. The simulation results are compared with Atomic Force Microscopy and Transmission Electron Microscopy experiments.

Keywords Flame spray pyrolysis · AFM force spectroscopy · Multiscale modelling · Nanoparticle agglomerates

1 Introduction

Many new technologies such as gas sensing, catalysis, electrochemical energy storage, or photodetection rely upon devices in which porous nanoparticulate films with characteristic thickness of a few micrometers are the active functional elements [1,2]. The performances of such devices are crucially dependent upon the structural and mechanical properties of the films, in particular their interparticle percolation paths (connectivity), the particles' surface accessibility by diffusing gases (porosity, tortuosity), and their response to handling steps including lamination or compaction. The relationships between external loading and changes of the internal architecture of the films are often more difficult to assess experimentally than via theoretical modelling. Therefore, a fundamental understanding of the interactions governing the mechanical behaviour of complex nanoparticle assemblies under ambient conditions is highly desired.

Cundall and Strack [3] first developed the discrete element method (DEM), which has since been improved with more and more sophisticated models capable of simulating granular systems with a high degree of precision and reasonable computational effort (Ref. [4] and references therein). However, only sporadically have DEM models been applied to simulate the behaviour of assemblies of particles with characteristic dimensions of the order of 10 nm or less [5–8]. This is due to the lack of precise knowledge about the elementary mechanisms of interparticle contact at this size scale. Contact models, however, need to accurately map physical and chemical effects at the particle-particle interfaces in order to predict the correct mechanical response of nanoparticulate systems.

A widely used approach to define contact models and to determine their parameters for DEM simulations relies on heuristic matching between experimentally measured and simulated macroscopic system properties [5,6,9]. The dif-

Electronic supplementary material The online version of this article (https://doi.org/10.1007/s10035-018-0799-9) contains supplementary material, which is available to authorized users.

✉ Lucio Colombi Ciacchi
colombi@hmi.uni-bremen.de

[1] Hybrid Materials Interfaces Group, Faculty of Production Engineering, Bremen Center for Computational Materials Science, MAPEX Center for Materials and Processes, University of Bremen, 28359 Bremen, Germany

[2] Leibniz-Institut für Werkstofforientierte Technologien - IWT, Faculty of Production Engineering, MAPEX Center for Materials and Processes, University of Bremen, 28359 Bremen, Germany

[3] Present Address: Product and Process Engineering Group, Department of Chemical Engineering, Delft University of Technology, 2628 BL Delft, The Netherlands

ficulty with this approach is that the coarse-grained potential terms and parameters used to reproduce the chosen experimental observables not always have a clear physical meaning. This may result in limited predictive capability and poor transferability of the models, especially at the nanoscale, where direct measurements of interparticle contact forces and friction are exceedingly difficult to perform.

In this work we take a different approach. We develop and parametrize a coarse-grained potential for the DEM simulation of polydisperse TiO_2 nanoparticle films under stress at ambient conditions (300 K, 1 atm, 50% r.h.) based entirely on all-atom molecular dynamic simulations. The accuracy of these simulations has been validated both qualitatively and quantitatively against Atomic Force Microscopy (AFM) measurements of interparticle forces in humid air presented in previous own studies [10,11]. The here-developed DEM contact model can be directly used for the investigation of the mechanical behaviour of TiO_2 nanoparticle assemblies, as we will show by reproducing the AFM force-distance curves collected when an AFM tip is put in contact and retracted from a TiO_2 nanoparticle film produced by means of flame-spray pyrolysis (FSP) [12].

Throughout the present paper we use the term 'assembly' to indicate a generic system comprised of a large number of nanoparticles (of the order of 10^4 to 10^5 per μm^3) structured according to a hierarchical architecture. The lowest hierarchical units are 'primary particles', with characteristic sizes spanning a relatively wide distribution of the order of 1–20 nm. As a result of the FSP process [13], primary particles are clustered together in 'aggregates', in which the particle-particle interactions are typically of covalent/ionic nature or of comparable strength. Such aggregates typically comprise a number of primary particles of the order of 1–100 [14]. Ensembles of mutually interacting aggregates are called 'agglomerates'. They are held together by the action of weaker forces arising from electrostatics, van der Waals, solvation or capillary effects [10,11]. Finally, we call 'films' extended assemblies with thicknesses of the order of 1–50 μm over surfaces of the order of several cm^2.

An example of TiO_2 nanoparticle agglomerates subjected to tensile strain by means of an AFM tip incorporated in a Transmission Electron Microscope (TEM) chamber is presented in Fig. 1. During progressive increase of the strain, the agglomerates undergo evident rearrangements, which are associated with particle-particle sliding, rolling and detachment events. To be able to predict the mechanical response of the strained nanoparticulate system, all of these elementary events need to be quantified in detail and mapped into adequate contact model elements, taking into account their dependencies on the particle size and environmental conditions, in particular relative humidity. Recently we have demonstrated that the normal particle-particle detachment forces under ambient conditions are crucially determined by

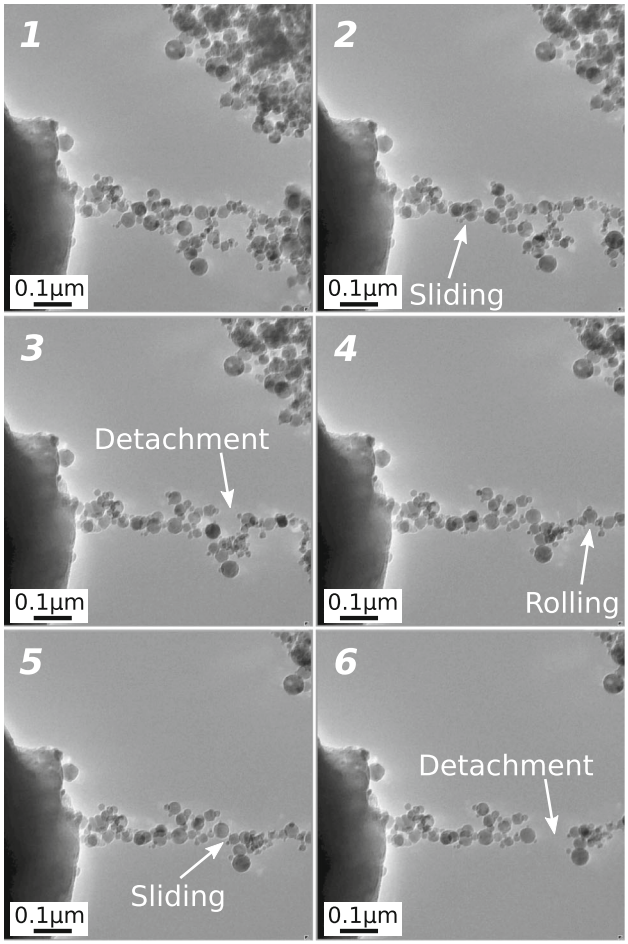

Fig. 1 Series of images from combined AFM/TEM experiments showing the rearrangement and detachment of particle contacts during the retraction of the AFM-tip [12]. A further selection of AFM/TEM experiments yielding a more comprehensive view on the particle rearrangements can be found in the Electronic Supplementary Material (Online Resources 5, 6, 7, 8, 9, 10)

the molecular properties of the water adsorbate layer on the particles' surfaces [10–12,15,16]. It remains to be investigated how the mutual particle-particle friction forces, which govern the sliding and rolling events shown in Fig. 1, are influenced by the atomic-scale roughness of the surfaces and the hydration layers trapped between the particles in contact. Given the very localized nature of the contact areas, we expect large deviations from the macroscopic friction behaviour, as suggested in a number of previous theoretical and experimental studies [17–22,24].

In the following we first present the theoretical framework of a novel particle-particle contact model for the coarse-grained simulation of TiO_2 nanoparticle assemblies with non-uniform size distributions. The quantification of the interactions is based upon all-atom MD simulations with the methods introduced in our previous work [10,11]. The so-obtained formulation and parametrization of the contact model is implemented in a DEM scheme, which we vali-

date against further MD simulations of small nanoparticle agglomerates, as well as AFM force spectroscopy experiments of entire nanoparticle films.

2 Formulation and parametrization of a DEM contact model

In this section we present the theoretical framework on which our DEM contact model is based, and parametrise the analytical force terms on the basis of all-atom molecular dynamics simulations, some of which were reported in detail in previous works [10,11]. We limit our development to the case of TiO_2 nanoparticles of different sizes (with radii of the order of 1 to 20 nm) interacting in an atmosphere with relative humidity of 50%. Under these conditions, the particles are covered by a water adsorbate layer with an average thickness $h = 0.41 \pm 0.03$ nm, which is independent of the particle size in the considered size range [11]. When two particles come in contact, their adsorbate layers interpenetrate, leading to a particle-particle overlap δ_n, as schematically presented in Fig. 2. The equilibrium distance between the particles is dictated by the balance between the long-range attraction force $\mathbf{F}_{\mathrm{na}}$ exerted by capillary and solvation effects (which include also the van-der-Waals contributions) and by the short-range steric repulsion $\mathbf{F}_{\mathrm{nr}}$ of both the surface terminal groups and the adsorbate water molecules trapped between the particles. The effect of electrostatic charging of the particles is negligible under the conditions investigated here, as addressed in Ref. [11]. Also, for particles of this small size and in the presence of water layers between them, we assume that friction arising from mutual torsional displacements can be neglected.

Under these conditions, the action of external forces and torques between two particles i and j results in three kinds of mutual displacements: (1) shifting along the normal direction $\mathbf{n}_{ij}$ connecting the particles' centres of mass; (2) sliding along the perpendicular, tangent direction $\mathbf{t}_{ij}$; (3) rolling with a relative rotation $\boldsymbol{\Delta\theta}$ of one particle in the reference frame of the other. All three kinds of displacements are associated with friction contributions, which arise both from direct interactions of the surface terminal groups and from dissipation within the adsorbed water. In particular, a rolling friction torque $\mathbf{M}_{\mathrm{r}}$ and a tangential friction force $\mathbf{F}_{\mathrm{t}}$ will act against the rolling angular velocity $\mathbf{w}_{\mathrm{r}}$ and the sliding tangential velocity $\mathbf{v}_{\mathrm{t}}$, respectively. A dissipative force $\mathbf{F}_{\mathrm{nd}}$ will also act against the velocity in normal direction $\mathbf{v}_{\mathrm{n}}$, damping the normal displacements off the equilibrium position of the particles in contact.

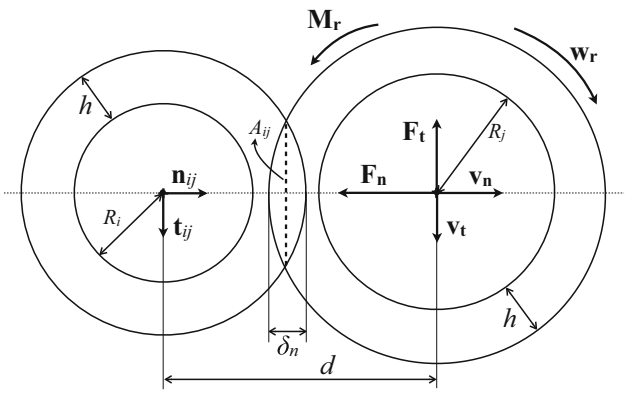

Fig. 2 Scheme of two particles with radii R_i and R_j interacting via a circular cross-section of area A_{ij} after overlap of their water adsorbate layers with thickness h, whose size with respect to the radii is exaggerated, for clarity. The symbols are defined in the text

In light of the above, the total force $\mathbf{F}_{ij}$ and the torque $\mathbf{M}_{ij}$ acting between the particles can be thus expressed as

$$\mathbf{F}_{ij} = \mathbf{F}_{\mathrm{na}} + \mathbf{F}_{\mathrm{nr}} + \mathbf{F}_{\mathrm{nd}} + \mathbf{F}_{\mathrm{t}} = \mathbf{F}_{\mathrm{n}} + \mathbf{F}_{\mathrm{t}}, \tag{1}$$

$$\mathbf{M}_{ij} = -\mathbf{F}_{\mathrm{t}} \times R_i^{aug} \mathbf{n}_{ij} - \mathbf{M}_{\mathbf{r}}, \tag{2}$$

where R_i^{aug} is the radius of the particle i augmented by half the thickness of the compressed water layer, as it will be clarified later in the paper.

This general form of a DEM contact model is in line with previous original formulations, in particular by Luding [9], with the important difference that in the present case the overlap between the particles is due to the interpenetration of the adsorbate layer rather than due to elasto-plastic deformations. Since we focus on hard ceramic nanoparticles, plasticity is not relevant for our case, and thus not considered. In the following sections we investigate the details of each force and torque contribution, performing all-atom MD simulations to rationalise them in the form of analytical expressions and determine the numerical parameters of such expressions whenever required.

2.1 Long-range attractive forces

As comprehensively shown in previous works [10–12], the attractive interaction $\mathbf{F}_{\mathrm{na}}$ can be modelled as the sum of capillary and solvation contributions acting along $\mathbf{n}_{ij}$:

$$\mathbf{F}_{\mathrm{na}} = -\left(F_{cap} + F_{solv}\right)\mathbf{n}_{ij} \tag{3}$$

The calculation of F_{cap} for different particle sizes has been undertaken in refs. [10,11]. In these works it has been shown that classical capillary theory can be employed to this aim, providing that one takes into account (i) the above-mentioned overlap of the surface adsorbed water layers; (ii) the dependence of the water surface tension on the humidity and particle size, and (iii) a contact angle of 0° between the water meniscus and the water-decorated particles.

The solvation forces can either be calculated as presented in detail in Ref. [10], taking into account the water density

distribution around nanoparticles immersed in bulk water and the average water/surface interaction forces, or, more simply, mapped onto a semi-empirical equation as proposed by Israelachvili [16,25]:

$$F_{solv} = F^0_{solv} \cos\left(\frac{2\pi(d - R_i - R_j)}{\sigma_{solv}}\right) e^{-\frac{d-R_i-R_j}{\sigma_{solv}}}, \quad (4)$$

where d is the distance between the centres of mass of the spherical particles. The decay length σ_{solv} and the force amplitude F^0_{solv} can both be fitted to match the force oscillations computed in MD simulations [10,11]. Our MD results for TiO_2 nanoparticles show that σ_{solv} is independent on the particle size, whereas F^0_{solv} depends weakly on the effective particle radius $R^* = 2R_iR_j/(R_i + R_j)$, in a way that can be linearly approximated to

$$F^0_{solv} = -11\ \text{nN} - R^* \cdot 2.4\ \text{nN/nm} \quad (5)$$

(see Online Resource 1, Supplementary Figure S1).

2.2 Dissipation in normal direction

The dissipative force in normal direction can be expressed as a classical damping term linearly dependent on the normal velocity

$$\mathbf{F}_{\text{nd}} = -\gamma_n \mathbf{v}_{\text{n}}. \quad (6)$$

In order to determine the damping coefficient γ_n, we perform all-atom MD simulations of two water-decorated particles facing each other. Several MD runs are performed starting with the particles at a distance larger than their equilibrium separation, first relaxing the water layers to form a stable meniscus (for about 0.6 ns), and then letting the system spontaneously relax to equilibrium at constant temperature.

The evolutions of the distances d between pairs of particles with either 4 nm or 8 nm radius are reported in Fig. 3. It can be seen that d quickly approaches equilibrium with a damped oscillatory behaviour, which can be well reproduced by the damping term above (Eq. 6) with a coefficient that depends quadratically on the effective particle radius:

$$\gamma_n = 0.5 \cdot 10^6\ \text{Ns/m}^3 \cdot R^{*2}. \quad (7)$$

2.3 Short-range repulsive forces

When two particles are compressed by an external normal force ($-F_N\,\mathbf{n}_{ij}$) below their equilibrium separation distance, they experience a repulsive force $\mathbf{F}_{\text{nr}} = F_{nr}\,\mathbf{n}_{ij}$. The repulsion originates both from the compression of the water layers trapped between the particles and the steric interactions between the surface's outmost atoms. To quantify F_{nr} we perform simulations in which particles of different size and shape are placed in contact with a flat TiO_2 surface and pressed towards it by action of a force F_N along the z axis perpendicular to the surface. The average position of z recorded in MD simulations is plotted as a function of the reaction force F_{nr}, which is equal in magnitude and opposite in sign to the sum of F_N and F_{na} (Fig. 4).

Fitting of the data to polynomial functions reveals that a ninth-order dependence describes the variation of F_{nr} with z very well over the whole range of distances and forces. However, such a stiff dependence leads to high instabilities in DEM simulations unless an extremely small time step is used, which would impede the simulations of entire particle films. For this reason, we chose to fit the data only in the region of forces smaller than 5 nN via a softer dependence of order 3/2, in line with often-employed Hertz stress models of compressed elastic spheres [26]. This dependence describes well the variation of F_{nr} in the region of a few Å around the equilibrium separation distance (Fig. 4), which is the region of interest in DEM simulations of particle films.

Consistently with this result, we can express F_{nr} as a function of the particle-particle overlap δ_n as

$$F_{nr} = k_n \delta_n^{\frac{3}{2}} \sqrt{0.5(R + h_n)^*}, \quad (8)$$

where k_n is the Hertzian contact stiffness and $(R + h_n)^*$ is the combined effective radius $2(R_i + h_n)(R_j + h_n)/(R_i +$

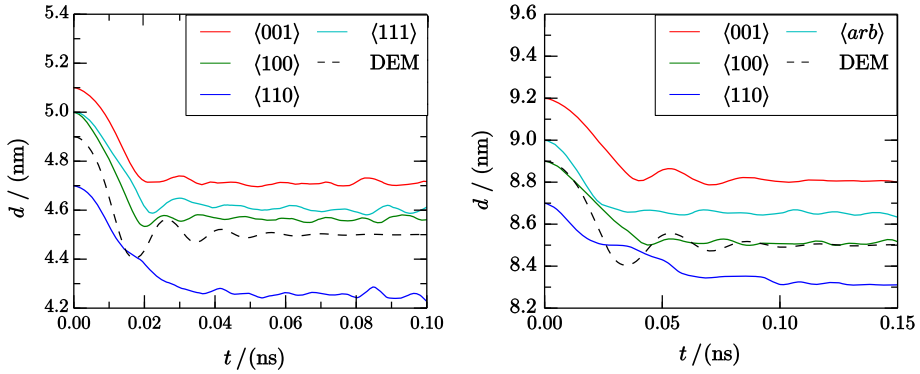

Fig. 3 Time evolution of the particle-particle distance d for pairs of particles with 4 nm (left) and 8 nm (right) radius, facing each other along different orientations (coloured continuous lines), during MD simulations started at distances larger than the equilibrium separation. The black lines are the results of DEM simulations using a linear damping term as described in the text (Eqs. 6 and 7) (colour figure online)

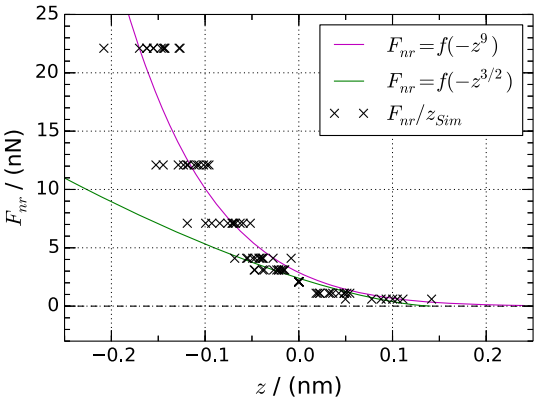

Fig. 4 Dependence of the repulsion force F_{nr} on the separation distance z between TiO_2 nanoparticles with radii of 4 nm and a flat TiO_2 surface obtained in several MD simulation runs (see Fig. 5). The z values are reported relative to the equilibrium separation for $F_N = 0$ in each simulation. The coloured lines show polynomial fits with exponents 9 (magenta) and 3/2 (green), as described in the text (colour figure online)

$R_j + 2h_n$). The parameter h_n is related, but not equal, to the water adsorbate thickness h that adds up to each of the nominal particle radii R_i and R_j, physically accounting for the particle overlap [10,11]. It represents the thickness of the compressed water layer between two particles in equilibrium, below the onset of repulsion. The value of h_n can be estimated by quantifying the difference in particle-particle separation distance between the equilibrium position ($F_N = 0$, $F_{nr} = -F_{na}$) predicted by many all-atom MD simulations of pairs of particles and the position at the absence of repulsion ($F_{nr} = 0$, $F_N = -F_{na}$). The resulting value $h_n = 0.88\,h$ (0.36 nm), which is used in our DEM model, best reproduces both this distance difference and the overall normal forces computed by all-atom MD.

The contact stiffness k_n is size-dependent, and can be calculated from the condition of equilibrium $F_{nr}(0) = -F_{na}(0)$, valid for the case of $F_N = 0$, applied to the MD simulations of pairs of particles in contact presented in Ref. [10,11]. Namely, the equilibrium overlap $\delta(0)$ is first determined from the pristine MD force-displacement curves. Then, $F_{na}(0)$ is computed as in Eq. (3) and the Hertzian stress model is used to back-compute k_n as

$$k_n = \frac{-F_{na}(0)}{\delta_n(0)^{\frac{3}{2}}\sqrt{0.5(R+h_n)^*}}. \tag{9}$$

The values of k_n obtained with this procedure vary slightly more than linearly between 20 and 45 GPa for particle sizes between 4 and 23 nm (See Online Resource 1, Supplementary Table S1). These values are much lower than the typical stiffness of TiO_2 (around 210 GPa [27]), but higher than the compressibility of water or ice (around 2 GPa [28]), which is fully consistent with compressing TiO_2 particles separated by an adsorbed water layer.

2.4 Tangential force and rolling torque

In this section we investigate the origin of the tangential friction force $\mathbf{F}_t$ and the rolling torque $\mathbf{M}_r$ acting between particles in contact. To this aim we perform all-atom MD simulations of particles dragged over an extended TiO_2 surface with different tangential velocities while applying to the particles different normal loads F_N (Fig. 5). In the simulations the particles are either allowed to rotate along the x axis while their center of mass is pulled along the y direction, which results in a rolling behaviour (Fig. 5, right), or their rotation is forcedly suppressed, resulting in a sliding behaviour (Fig. 5, left). During the simulations, we record the module of the tangential force F_t that is required to keep the particles moving at constant speed.

The resulting force-displacement curves for the exemplary case of particles with a radius of 4 nm pulled at 1 m/s are reported in Fig. 5. Both during sliding and during rolling the curves exhibit a typical stick-slip behaviour. This is common for the friction behaviour of surfaces with roughness in the atomic scale (of the order of 0.1 nm), as already shown theoretically [18,29–32] and experimentally [24,30,33,34].

As expected, for the case of sliding the force peaks are significantly higher and the periodic force oscillations are more clearly pronounced than for the case of rolling. This is due to the fact that a sliding motion is associated with the contemporary breaking and reforming of a larger number of bonds than during rolling. We approximate the observed sliding behaviour with a regular saw-tooth curve, whose peak value $F^S_{t,max}$ and period λ_t correspond to the average values of the maxima and oscillation periods of the most prominent peaks in the force-displacement curves (see Appendix, Sect. 5 for further details). Instead, the rolling behaviour is simplified by considering a constant friction force $F^R_{t,max}$ with a value equal to the simulated average peak forces.

We find that λ_t is independent of the applied normal load F_N, with a value of approximately 0.5 nm (See Online Resource 1, Supplementary Figure S2). Moreover, very similar force-displacement curves are obtained at different pulling speeds (See Online Resource 1, Supplementary Figure S3), suggesting that the influence of the drag velocity on both the magnitude and the overall behaviour of the tangential forces is negligible [31,32,35,36]. The only important dependence is the one of the maximum force values $F^S_{t,max}$ and $F^R_{t,max}$ on the normal load F_N, which is summarised in Fig. 6.

The computed dependence between F_N and F_t is clearly non-linear, in contrast to the case of macroscopic friction (Amontons' law). Rather, for atomic-scale asperities within a single contact, the peak friction forces depend linearly on the contact area A_{ij} between the overlapping particles i and j (see Fig. 2), as reported in many theoretical [22,23,30,31,37] and experimental works [30,33,38–40]:

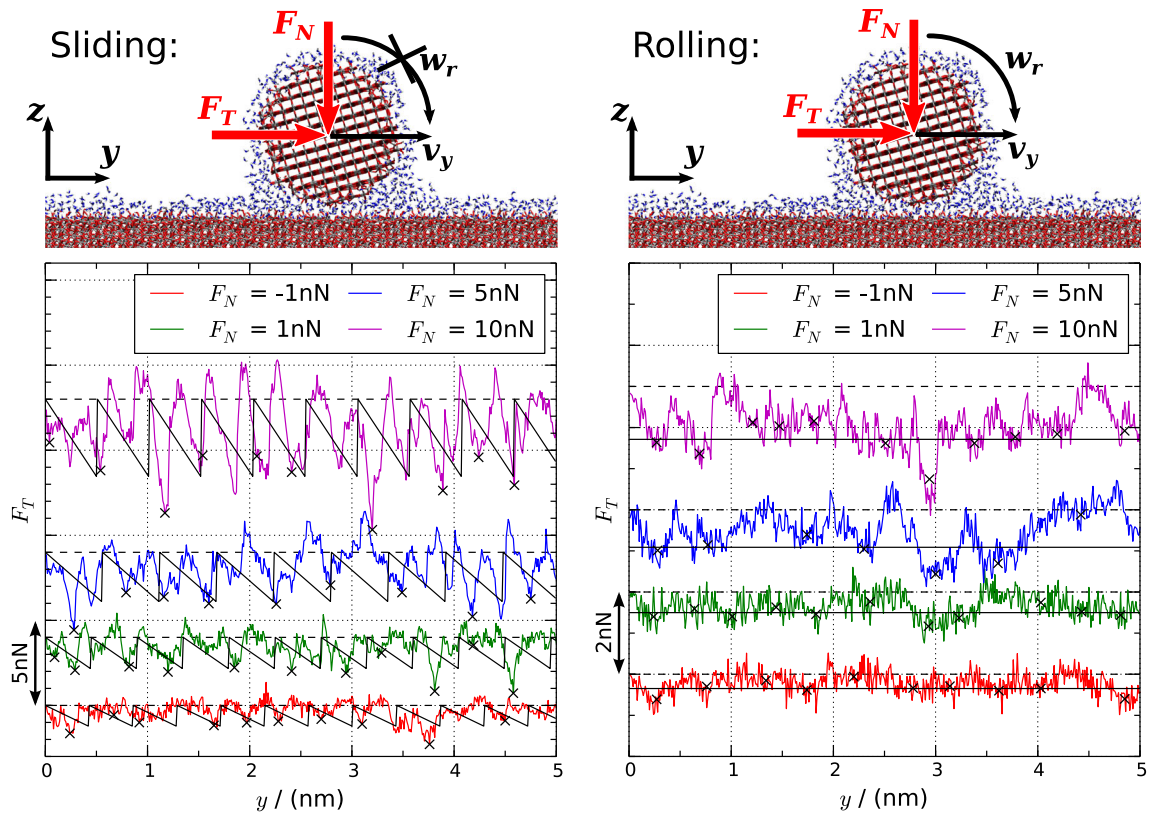

Fig. 5 Top: all-atom MD snapshots and scheme of the forces and displacements acting on a particle with 4 nm radius during a tangential sliding (left) or rolling (right) movement on a slab. Bottom: Respective tangential force displacement curves at a pulling velocity of 1 m/s and different normal loads F_N for sliding (left) and rolling (right) movement. The force curves are shifted on the y-axis for clarity, with the tangential force of 0 nN marked by a dashed black line in each case. The black crosses denote the fitted local maxima of the force curves and the black continouus lines show the respective coarse grained force models

$$F^S_{t,max} = \tau_S A_{ij}; \quad F^R_{t,max} = \tau_R A_{ij}, \tag{10}$$

where τ_S and τ_R are the shear stiffnesses for the sliding and rolling case, respectively. The contact area A_{ij} depends on the particle-particle distance d (or, equivalently, on the overlap distance δ_n) and can be calculated as:

$$A_{ij} = \pi \left[R_i^2 - \frac{\left(R_i^2 - R_j^2 + d^2\right)^2}{4d^2} \right]. \tag{11}$$

Consistently with the interaction models presented so far, the parameters τ_S and τ_R can be determined as follows. For each applied normal load F_N, the reaction force F_{nr} is recorded as an average from the sliding/rolling MD simulations (Fig. 5). Using the already determined values of k_n, we can now use Eq. (8) to compute the overlap distance δ_n and, from the latter, the contact area A_{ij} of a geometric sphere/plane intersection model. With the resulting values of A_{ij} we then fit the data points presented in Fig. 6 using Eq. (10), obtaining excellent agreement between the original data and the fit (continuous lines in Fig. 6).

The values of the sliding shear stiffnesses τ_S obtained for the cases of 4 and 8 nm particles dragged over a plane surface are 0.76 and 0.57 GPa, respectively. They are within the range of shear stiffness reported for atomic-level friction (between 0.3 and 0.9 GPa [33,38,39]). In comparison, the corresponding values of rolling shear stiffness τ_R are considerably smaller, amounting to 0.23 and 0.13 GPa for our 4 and 8 nm particles, respectively. The differences between these values, which should be independent on the particle size, originate from the uncertainties of the MD simulations, which represent only a possible case among many different orientations, terminations, roughnesses, etc. However, we note that using spherical particles in our simulations is a reasonable approximation in the presence of water adsorbate layers connecting the particles and effectively smoothing the roughness of the particles at the nanometer scale. In this case, the peak forces experienced during rolling become dominated by sudden rearrangements of the hydrogen bond network rather than by direct interactions between surface

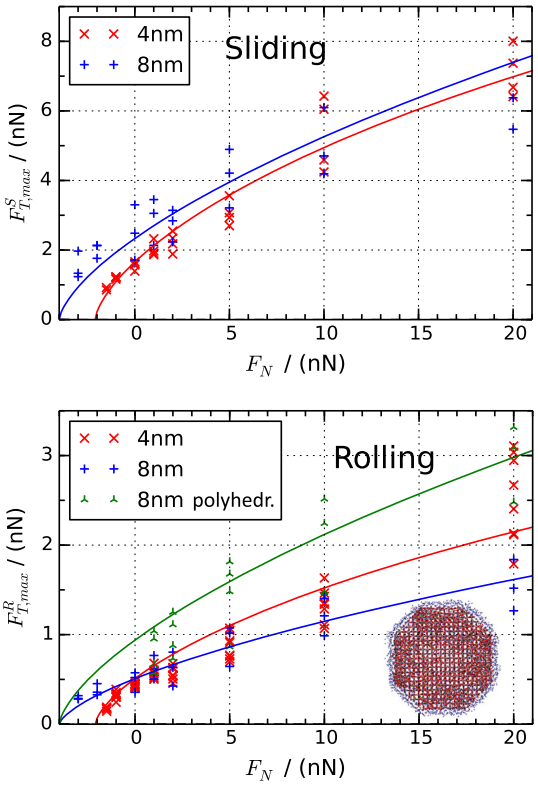

Fig. 6 Average of the peak tangential forces from the sliding (top) and rolling (bottom) simulations as shown in figure 5 against the respective applied load for different particle sizes and orientations. The continuous lines represent fits to the forces by assuming a linear relationship between the tangential forces and the contact area using the Hertzian stress relation between the normal force F_n and the normal overlap δ_n with a contact stiffness of k_n = 24.5 GPa and k_n = 33.7 GPa for 4 and 8 nm particles, respectively. The inset shows the atomistic model of the polyhedral 8 nm particle used for the rolling simulations

atoms. In fact, using a polyhedral 8 nm particle exhibiting a total of 32 edges (see inset of Fig. 6, to be compared with the TEM images of actual particles in Supplementary Figure S4 of Online Resource 1), a rolling shear strength τ_R of 0.23 GPa is obtained, matching the value obtained for spherical (although with atomic-scale asperities) 4 nm particles.

From the results of the MD simulations above we can now express the tangential friction force $\mathbf{F}_t$ as a spring-slider model in line with the work of Mindlin and Deresiewicz [41]:

$$\mathbf{F}_t = -\tau_S A_{ij} \left(\frac{\delta_t}{\lambda_t} - \left\lfloor \frac{\delta_t}{\lambda_t} \right\rfloor \right) \mathbf{t}_{ij}, \tag{12}$$

where δ_t is the relative displacement of two particles along the tangential direction $\mathbf{t}_{ij}$ and $\lfloor x \rfloor$ denotes the floor function of x. This expression leads to the saw-tooth curve with period of displacement λ_t displayed as a black solid line in Fig. 5, left panel. In the DEM model the (size-independent) value we use for the sliding shear stiffness τ_S is 0.65 GPa, which

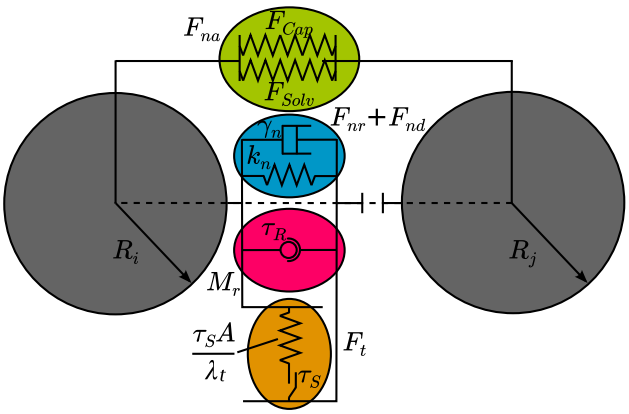

Fig. 7 Schematic representation of the developed DEM contact force model

averages the values obtained from the exemplary simulations for 4 and 8 nm particles (Fig. 6).

The MD simulations of the particles' rolling behaviour allow us to express the rolling torque acting between a pair of particles i and j as a simpler slider model [42,43]:

$$\mathbf{M}_r = 0.5(R + h_n)^* \tau_R A_{ij}, \tag{13}$$

where, as before in Eq. (8), the radius of the two dry particles is augmented by the thickness h_n of the compressed adsorbed water layer at 50% relative humidity. The chosen value of the rolling shear stiffness τ_R is 0.25 GPa, which is roughly equal to the upper range of values obtained in our MD simulations for spherical and aspherical particles (Fig. 6), in order to account for the mostly irregular shapes of primary nanoparticles in TiO_2 films obtained by means of flame spray pyrolysis (see for instance Fig. 1 and Online Resource 1, Supplementary Figure S4).

2.5 Summary of the developed DEM contact model

The results of the previous subsections, together, represent a novel DEM contact model that allows for the simulation of ensembles of TiO_2 nanoparticles under external mechanical load, as long as the particles are small enough (radius well below 1 μm) so that they can be safely approximated as rough spheres in the absence of gravity. The interactions in the model are depicted schematically in Fig. 7.

The normal attractive force F_{na} (light green) consists of capillary and solvation forces [10,11] and acts on the particles as long as their separation is below the critical distance corresponding to the formation of a capillary neck (Eq. 3). The repulsive and dissipation normal contact terms $F_{nr}+F_{nd}$ (light blue) correspond to a non-linear spring-dashpot model (Eqs. 6, 8, 9). The tangential friction term F_t (orange) consists of a linear spring-slider model (Eq. 12), in which the maximum force sustained before activation of the slider is

Table 1 Parameters used in this work for the discrete element method simulations

Solvation force decay length	σ_{solv}	0.21 nm
Solvation force amplitude	F^0_{solv}	Eq. (5)
Normal relative damping constant	γ_n	Eq. (7)
Adsorbate layer thickness	h	0.41 nm
Compressed layer thickness	h_n	0.36 nm
Normal contact stiffness	k_n	Eq. (9), Table S1
Sliding sawtooth wavelength	λ_t	0.50 nm
Sliding shear stiffness	τ_S	0.65 GPa
Rolling shear stiffness	τ_R	0.25 GPa

computed according to Eq. (10). The rolling friction torque M_r (red) consists of a pure slider model (Eqs. 10, 13). The last four terms are only active when the particles are in tight contact, *i.e.* whenever δ_n and thus A_{ij} are larger than zero.

The values or size-dependencies of all numerical parameters estimated via the presented MD simulations and used in the DEM simulations in the next sections are summarised in Table 1. The normal and tangential DEM force-displacement curves are shown in Fig. 8.

The critical timestep under which numerical stability of the integration algorithm in DEM simulations is guaranteed can be estimated from calculation of the so-called Rayleigh time according to Ref. [44], leading to a value of 10^{-12} s. Therefore, to be on the safe side, in our DEM simulations we use a timestep half as large, namely: $\Delta t = 0.5$ ps.

3 Validation of the DEM model

In this section we validate the DEM model and its parametrization presented above against all-atom MD simulations.

3.1 DEM and all-atom MD stretching of a small nanoparticle agglomerate

First, we investigate an agglomerate consisting of 14 TiO_2 particles with radii between 4 and 10 nm (Fig. 9, panel **1**), resembling typical particle chains observed in TEM images (see Fig. 1). Using either DEM or full-atom MD, the agglomerate is stretched by action of an external harmonic constraint applied to the center of mass of the two last particles at one extreme of the agglomerate, while the center of mass of the two last particles at the opposite extreme is kept fixed. The constraint is pulled at the constant speed of 5 m/s (corresponding to a strain rate of $5 \cdot 10^7\,\mathrm{s}^{-1}$ since our system is about 100 nm in length) while the reaction force F_{pull} acting on the agglomerate is recorded as a function of the pulling distance z. Such an exceedingly large strain rate is not uncommon in steered MD simulations [10,45], and needs to be used here in order to be able to compare the DEM results with an all-atom model.

As can be seen in Fig. 9, both the obtained trajectory and the noticeable force peaks originating from sliding/rolling or particle-particle detachment events agree remarkably well in the two independent simulation methods, especially if the experimental value of the water surface tension γ rather than the value predicted by the TIP3P water model is used. The only major difference is the less abrupt breakage of particle/particle contacts in the atomistic model in comparison with the DEM results, which is primarily due to the formation of long (and metastable) necks of water molecules at large particle-particle distances. This out-of-equilibrium effect is particularly strong at the large strain rate used in our simulation, and is not present in the DEM model, where the length of the capillary neck is fixed *a priori* (see Fig. 8, left panel). Moreover, the purely two-body DEM model formulation does not consider cooperative (non-linear) interaction effects between multiple particles and the possible accumulation of water molecules in the junction regions between them [46], which can lead to a slightly more pronounced and longer-ranged capillary action in the all-atom simulations.

3.2 AFM pulling simulations of whole nanoparticles films

As a further test for the predictive power and validity of our DEM model, we compare the forces and trajectories obtained

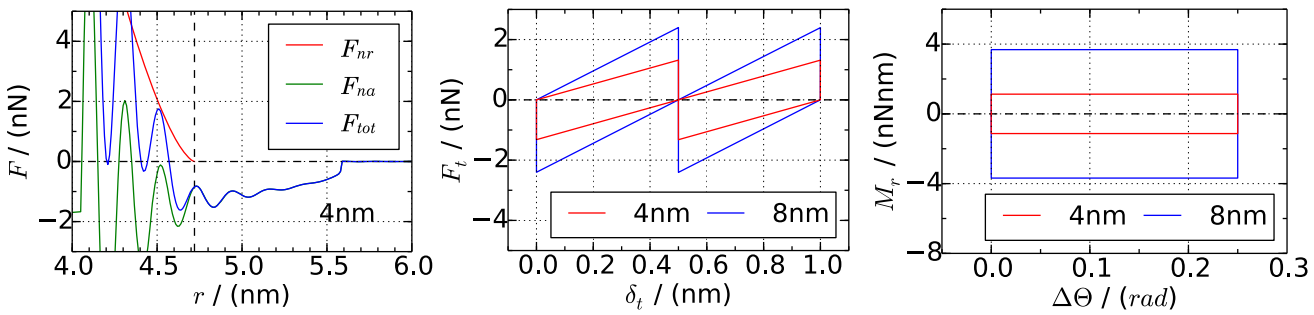

Fig. 8 Force-displacement curves in the discrete element method simulations for relative normal (left), tangential sliding (middle) and rolling (right) movement resulting from the developed contact model at 50% humidity

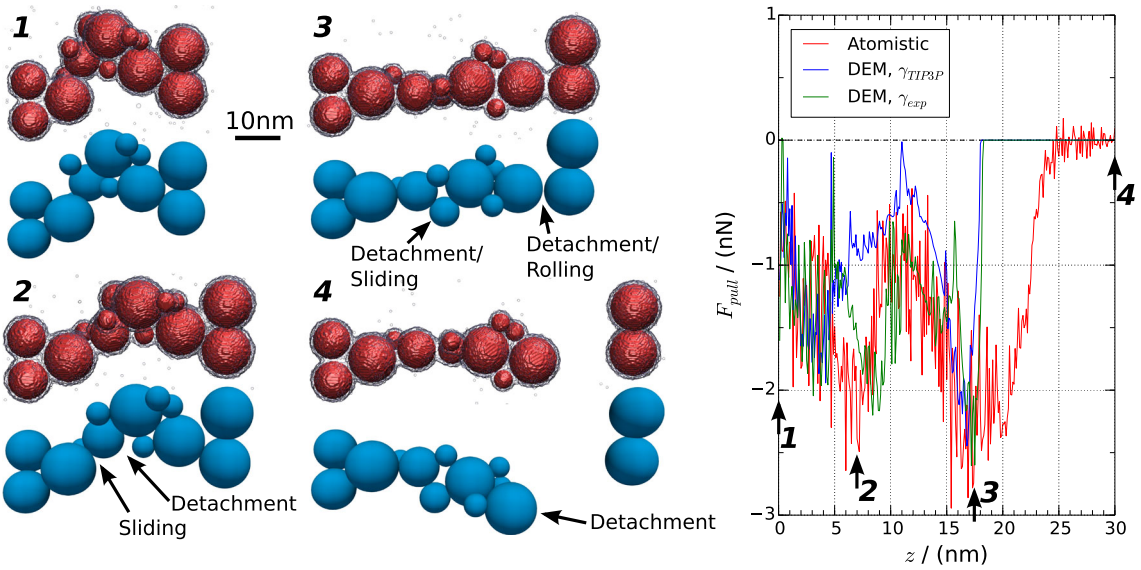

Fig. 9 Comparison of the particle trajectory (left) and of the pulling forces (right) in simulations of an agglomerate response to mechanical stretching using all-atom MD (upper trajectory panels; red curve) and DEM simulations (lower panels; green and blue curves). The DEM forces are computed using either the experimental water surface tension γ (green curve) or the value predicted by the TIP3P water model used in the atomistic simulations (blue curve). In both cases, the weak dependence of γ on the particle size found in Ref. [11] is taken into account. The z positions of the trajectory snapshots displayed on the left are marked by the respective numbers in the force displacement curve. The entire particle trajectory can be found in the Electronic Supplementary Material (Online Resource 2) (colour figure online)

in actual AFM experiments probing the tensile response of nanoparticle films with DEM simulations of a corresponding model setup. For this purpose we first construct a film model containing 2×10^5 primary particles in a periodically repeated simulation box. Here we take particular care ensuring that the model reproduces the correct experimental primary particle size distribution and porosity (98%), as shown in previous works [47,48]. Moreover, consistent with experimental findings [14,49–52], the primary particles in the film are clustered together in aggregates which are kept rigid in the DEM simulations. Further methodological details are reported in the Appendix (Sect. 5).

The film is first relaxed to equilibrium in a damped-MD simulation. Then, a model of a pyramidal AFM tip with a side length of 0.8 μm is approached towards the nanoparticle film with a speed of −0.5 m/s, until the repulsive force acting on it reaches a value of approximately 2 nN, which is a typical experimental AFM setpoint force [12]. Afterwards, the velocity of the tip is slowly reversed from −0.5 to +0.5 m/s within a timespan of 0.2 μs (which minimise spurious inertial responses of the system) and the tip is retracted at constant speed until complete detachment and rupture of the film.

One typical obtained trajectory and five exemplary force-displacement curves are reported in Fig. 10. During the pulling trajectories, particle aggregates firmly attach to the AFM tip and are progressively pulled out of the film, whose structure undergoes a series of local rearrangements associated with particle-particle rolling, sliding and detachment events, as expected. The observed transfer of nanoparticle aggregates from the film to the tip (snapshots **3** and **4** in Fig. 10) reproduces qualitatively well the experimental reality, as reported in Ref. [12]. Also the resulting force-displacement curves are, overall, consistent with the results of actual AFM experiments. In particular the total displacements until final rupture (about 1 to 2 μm) and the heights of the final detachment peaks (1 to 3 nN) agree remarkably well with the corresponding experimental values. Only the maximum peak force is slightly overestimated in some of the simulations, reaching up to 20 nN while the experiments remain within about 10 nN. Moreover, the simulated curves appear more rough and the local peaks less pronounced than in the experiments, although this may depend on the instrumental sensitivity.

In Fig. 11 we show selected snapshots of the DEM trajectory highlighting the events taking place in the film immediately before the force peak marked with **3** in Fig. 10. Importantly, the trajectory is qualitatively consistent with the characteristic chain rearrangements before particle-particle detachments observed in AFM/TEM experiments (see Fig. 1). We note that it is difficult to link the individual events before final detachment to precise features in the force-displacement curve, since the complex connectivity of the film is associated with non-trivial distributions of the forces within it. On the other hand, it is reassuring to see that the magnitude of the final force peak (3 nN) is perfectly consistent with the contact forces between pairs of particles both in previous AFM experiments and in all-atom MD sim-

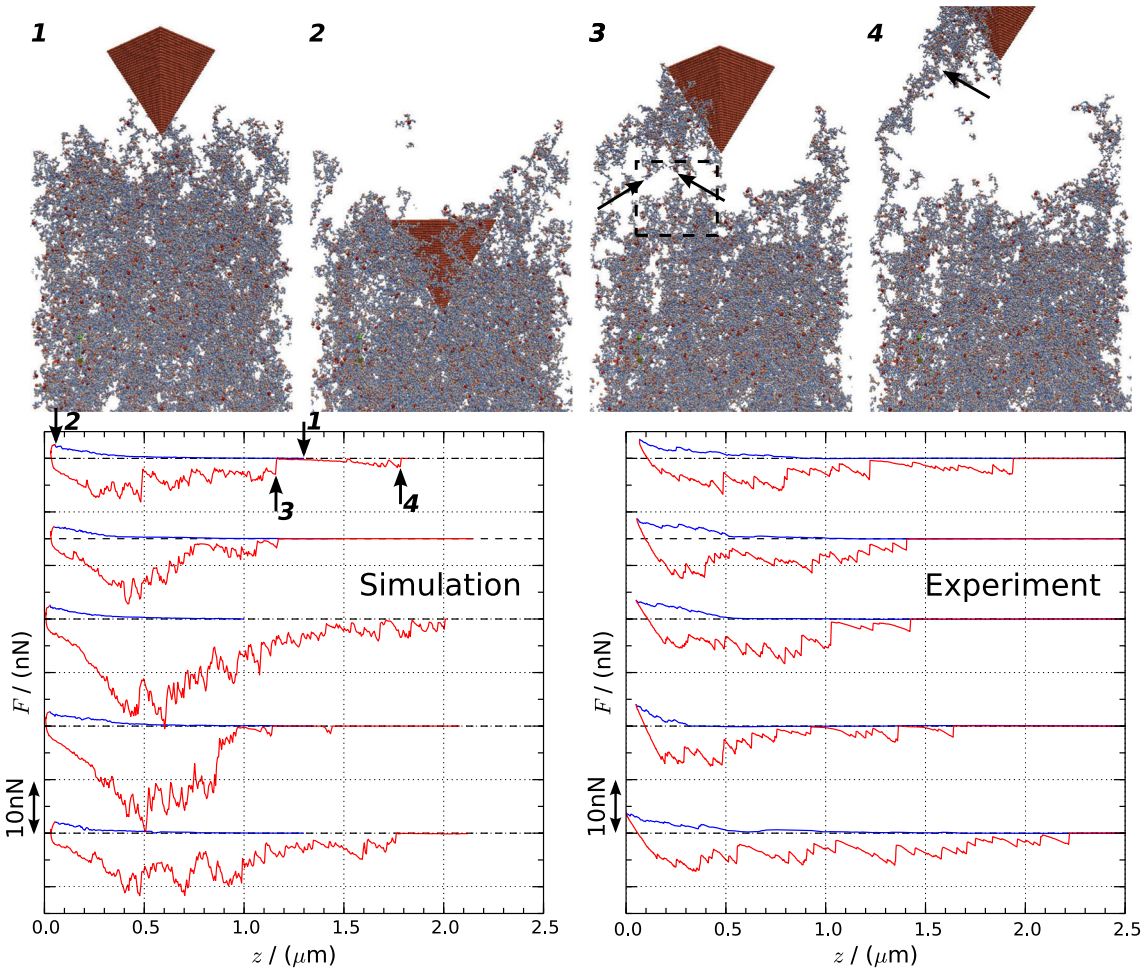

Fig. 10 Comparison of typical force-displacement curves from AFM force spectroscopy experiments (bottom right) with force-displacement curves from DEM simulations (bottom left), together with representative snapshots from one simulation (top), labelled with numbers in the corresponding curve. The blue lines represent the AFM tip approach and the red lines the tip retraction. The curves are shifted along the y axis for clarity. The particles are coloured according to their sizes from blue (2 nm) to red (25 nm). The approximate sites of particle-particle detachment events are marked with black arrows. The black dashed square highlights the region shown in detail in Fig. 11. The whole trajectory can be found in the Electronic Supplementary Material (Online Resource 3) (colour figure online)

ulations [10–12], including those presented in the previous section (Fig. 9).

4 Discussion, conclusions and outlook

In the present work we have shown that DEM simulation of the mechanical behaviour of TiO_2 nanoparticle films under external mechanical stress is feasible with our newly developed contact model. This has been formulated and parametrized on the basis of all-atom MD simulations [10–12], which, in turn, make use of interaction potentials constructed on the basis of the TiO_2 properties and surface chemistry predicted by quantum mechanics [53,54]. The coarse-graining of interactions into a mesoscopic contact model enables the simulation of systems with sizes comparable to those accessible by AFM and combined AFM/TEM experiments. In this way, the interpretation of these experiments in terms of individual events (rolling, sliding, detachment) leading to the rearrangement of nanoparticle chains in stressed films becomes possible.

4.1 Size and time scale issues

Naturally, the presented simulations are still limited as far as the system size is concerned. The dimensions of our film model are only about $1.5 \times 1.5 \times 3.0\ \mu m^3$, whereas experimentally produced films reach a thickness of approximately 20 μm [55]. This disparity results in a smaller penetration depth of the AFM tip during the simulations compared to the experiments, and especially in spurious effects on the computed force-distance curves due to the applied periodic

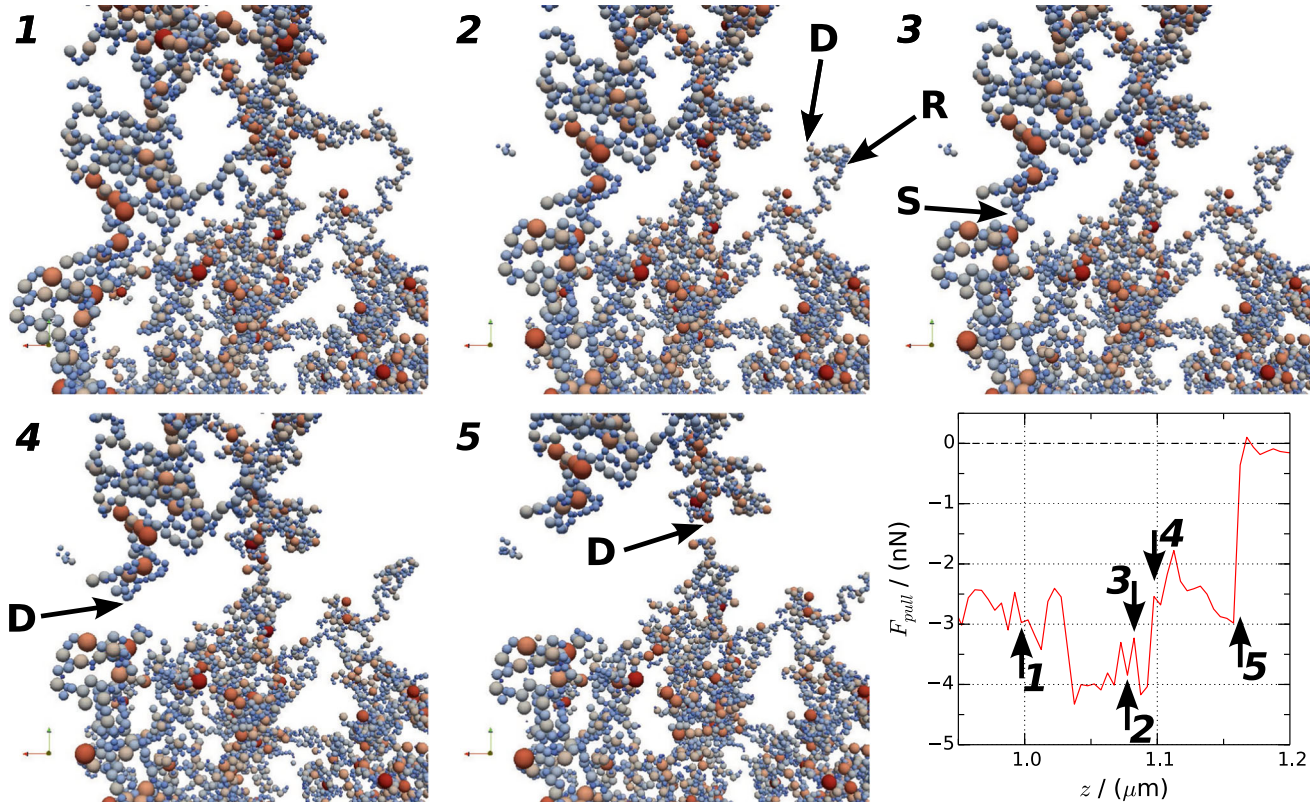

Fig. 11 Details of the rearrangements in the nanoparticle film during one of the AFM simulations in Fig. 10 (snapshots 1 to 5) along with the corresponding features in the force-displacement curve during pulling (graph). Particle-particle detachments are marked with *D*; sliding events with *S*; rolling events with *R*. Colour code as in Fig. 10. The whole trajectory can be found in the Electronic Supplementary Material (Online Resource 4)

boundary conditions. In particular, we think that such effects are primarily responsible for the overestimation (by up to a factor of two) of the maximum pulling forces in comparison with force spectroscopy experiments. Another issue is the much higher tip velocity in the simulations (here 5×10^{-1} m/s) compared to experiments (5×10^{-6} m/s). While we have taken care to perform the simulations at a velocity at least ten times smaller than the critical velocity at which non-equilibrium effects start playing an important role [10,11,45], still the inertia induced by the very high loading rate ($5 \times 10^{6}\,s^{-1}$ for systems with a characteristic length of 100 nm) may affect in a non-negligible way the elastic energy stored in the films. For instance, it may lead to an effective increase of their stiffness because the system does not have enough time to distribute the applied local stress.

4.2 Description of particle aggregates

Another limitation of our employed film models is the approximate description of particle aggregates. The particle-particle binding strength within such aggregates, comprised of a few tens of primary particles clustered together, has been shown to be much higher than the one between particles belonging to different aggregates, which is governed by the water adsorbate layers [14,49–52]. However, keeping the aggregates completely rigid probably represents an overestimation of the true bonding strength, especially with respect to the (correctly described) contact forces between hydrated particles. The physical/chemical nature and the mechanical properties of the bonds within aggregates should be addressed in future works, in order to improve the prediction of particle chain rearrangements, in particular taking into account the flexibility and rupture strength of inter-aggregate bonds.

4.3 DEM model parametrization

As far as the DEM model parameterization is concerned, we have taken great care to ensure internal self-consistency of all parameters and best-possible prediction of the forces and distances computed with all-atom MD. In particular, we would like to stress the tight correlation between the compressed water layer thickness h_n, the contact stiffness k_n and the shear stiffnesses τ_N and τ_R. Only the appropriate combi-

nation of these parameters is able to reproduce the delicate balance between normal attraction/repulsion forces on one side and tangential friction forces and momenta on the other side. The two effects are strongly correlated via the overlap distance δ_n, on which the contact area A_{ij} and thus the rolling/sliding friction directly depends (Eq. 10).

Noteworthy to this respect are the obvious deviation of the microscopic friction from the macroscopic behaviour reflected by Amonton's law, and the pronounced stick-slip behaviour of the tangential friction forces, which we have implemented in our DEM model via a linear sawtooth function. Surprising, to some extent, are the negligible dependencies of $\mathbf{F}_t$ and $\mathbf{M}_r$ on the relative tangential velocities between particle pairs, at least in the velocity regime of interest for nanoparticle films under non-impulsive mechanical load. This has allowed us to implement a single damping term acting only in normal direction in the DEM model. We note, however, that the initial structural relaxation of large nanoparticle film models must be performed very carefully, since precisely the lack of tangential damping could lead to catastrophic instabilities when the particle positions are far from equilibrium. This is due to the fact that the algorithm used to construct the film model does not take into account the DEM interactions, which would be computationally too expensive. For this reason, it is recommendable to perform an initial extensive minimization with a global dissipation term switched on (as if the system were immersed in a highly viscous liquid) before carrying out dynamical simulations.

4.4 Conclusions

In conclusion, we have presented a contact model that is adhesive, non-linear, hysteretic, and not plastic. Adhesion results from the action of adsorbed water, both through capillarity and solvation. Hysteresis derives from the dissipation terms associated with normal displacement, sliding tangential displacement and rolling. Further dissipation during the DEM simulations may be introduced with activation of an overall viscous term to mimic the effect of the environment, which also acts as an effective thermostat and prevents build-up of kinetic energy in the system. In our simulations, this is done only in the first equilibration stage. The non-linearity in the model originates both from the Hertzian elastic compressibility with exponent 3/2 and the dependence of the tangential friction forces on the contact area rather than on the normal force. Since the model is specifically designed to simulate nanoparticulate ceramic materials, plasticity is not relevant.

The general form of the DEM model expressed by Eqs. (1) and (2) is common to well-known existing models, such as the one originally proposed by Luding [9], which implements a classical sliding/sticking friction behaviour. However, the treatment of adhesion, compression and friction with non-linear terms instead of piecewise-linear terms with history-dependent normal stiffness is different, and we neglect here the effect of torsional resistance. Given the varied origins of non-linearity in our model, it is also conceptually different from the model of Ooi and collaborators [56], which relies on the introduction of a single parameter (the exponent of a power law) to smoothly vary the compression stiffness with increasing particle-particle overlap. It remains to be validated how these different models perform in predicting the response of particle films under the action of complex mechanical loading, for instance during the lamination of FSP-produced coatings [55].

4.5 Outlook

In the near future, the here-presented DEM model should be expanded to enable the simulations of other materials and other environments, e.g. adsorbates different from water. We believe that the knowledge about the fundamental interactions that we have acquired for the TiO_2/water system could be exported with relatively little effort, provided that adequate all-atom force-field potentials become available to perform the required reference simulations. Also, including in the DEM model information about particle shapes, rather than only the surface roughness via averaged shear-stiffness parameters, would be a big step forward for the simulations of a variety of crystalline nanoparticle systems. Finally, an increase of the simulation speed is necessary to reach system sizes and simulation times even closer to experimental reality. A first improvement in this direction would be a simplification of the explicitly computed particle-particle interactions in the contact model, or the integration of larger nanoparticle aggregates into single coarse-grained entities.

Electronic Supplementary Material

Electronic Supplementary Material is provided. This contains the Supplementary Figures S1, S2, S3, S4 and the Supplementary Table S1 cited in the text (Online Resource 1); three videos showing the results of MD and DEM simulations which are presented as snapshots in Figs. 9, 10, 11 (Online Resources 2, 3, 4); six videos showing AFM/TEM experiments of the stretching of TiO_2 nanoparticle chains, as presented in Fig. 1 (Online Resources 5, 6, 7, 8, 9, 10).

Acknowledgements We acknowledge fruitful discussion with S. Luding (University of Twente, The Netherlands) and M. Kappl (MPI for Polymer Research Mainz, Germany). The AFM/TEM investigations have been performed by S. Salameh during a research stay in the group of J.W. Seo (KU Leuven, Belgium). This work has been funded by the DFG within the SPP 1486 "Partikel im Kontakt" (Grants CO 1043/3 and MA 3333/3). Computational time has been provided by the HLRN supercomputing centre at Hannover and Berlin, Germany.

Compliance with Ethical Standards

Conflict of Interest The authors declare that they have no conflict of interest.

5 Appendix

In this Appendix we summarise the experimental as well as all computational and methodological details concerning the performed MD and DEM simulations.

5.1 AFM experiments

Highly porous TiO_2 nanoparticle films on mica substrates are produced using a flame spray reactor as described in detail in our previous works [13,14]. Force-displacement curves for the detachment of single agglomerates from the film are measured with an Atomic Force Microscope (Nanowizard 3 from JPK) under ambient conditions (relative humidity about 50%, temperature about 21 °C), using Si_3N_4 cantilever (DNPS from Bruker) with a spring constant of approximately 0.16 N/m, as determined from the thermal noise method [57]. The AFM is placed on a vibration isolation table (i4 from Accurion) inside an acoustic hood. To account for statistical significance, several force curves with a cantilever speed of 2 μm/s and a setpoint of 2.5 nN are collected by force mapping with 64 measurement points in an area of 2 μm^2. The dynamical agglomerate behaviour under strain is imaged using a combined AFM/TEM set-up with an Si_3N_4 cantilever of spring constant 5.3 N/m. These in-situ investigations are performed inside a Phillips CM 200 FG transmission electron microscope equipped with an AFM/TEM holder (Nanofactory Instruments AB) and with a column vacuum of approximately 10^{-6} mbar.

5.2 All-atom MD simulations

All-atom TiO_2 nanoparticle models of different sizes, shapes and with surface-adsorbed water corresponding to a relative humidity of 50% are created as described in detail in refs. [10–12]. This results in nanoparticles preserving the TiO_2 stoichiometry, but terminated with OH groups as a consequence of a thought-process of dissociative water adsorption, which saturates under-coordinated Ti and O sites with OH and H, respectively. An extended TiO_2 surface slab model with nanometer-scale roughness and size of 16×14 nm^2 is created via cleavage of an infinite TiO_2 single rutile crystal in the ⟨213⟩ lattice direction, subsequent surface relaxation, annealing and hydroxylation, similarly as for the particle models. The choice of the ⟨213⟩ direction is arbitrary; any combination of relatively large Miller indices would be suitable, as long as it leads, after annealing and termination with OH and H, to a non-periodic series of asperities and grooves on the size-scale of 0.1 to 1 nm. The Ti-O interactions are described by a modified Matsui/Akaogi force field [53], water molecules are described by the TIP3P model [58], and the interactions between water and TiO_2 by the force field of Schneider et al. [54]. All MD simulations are performed using LAMMPS [59] within the NVT ensemble at 300 K, using a Berendsen Thermostat, a timestep of 1 fs, a force cutoff of 12 Å for the van-der-Waals interactions and a particle-particle particle-mesh long-range solver for the Coulomb interactions.

In the MD simulations of single particles dragged tangentially over the TiO_2 surface, the particle/surface systems are first relaxed for 1 ns, then a harmonic constraint with a spring-stiffness of 160 N/m is applied to their centres of mass and moved at constant speed (0.1 to 1 m/s in different simulations) over a distance of 5 nm, while the atom positions of the slab are kept fixed, except for the terminal OH atoms and the adsorbed water molecules, which are free to move. The dragging force is recorded every 10^{-6} nm and averaged over 10^4 datapoints, giving a single force value every 0.01 nm. The angular momentum acting on the particle is set to zero at every time step in the sliding simulations, while it is unconstrained in the rolling simulations. The largest local maxima of the force-displacement curves obtained in these simulations are selected as in other works [30,33]. Namely, first the as-recorded curve is smoothed using a low-pass smoothing function with a cut-off frequency of $f_{cut} = 2.8$ nm^{-1}. The peak forces and peak positions of the smoothed function are then determined analytically. Finally, the maxima of the pristine curve nearest to the positions of the maxima of the smoothed forces are located. Averaging the force peak values and the spacings between the peaks leads the mean values of $F^S_{t,max}$ and $F^R_{t,max}$, as well as the period λ_t.

In the all-atom MD simulations of the nanoparticle agglomerate, 14 particles of different sizes are placed in contact and relaxed within 2 ns, keeping fixed the positions of the four outermost particles. The particles are created as (irregular) hollow spheres with a shell thickness of 1 nm, which considerably decreases the computational effort with no effect on the interparticle contact forces. The pulling force is exerted via a harmonic constraint with a spring-stiffness of 160 N/m moving at the constant speed of 5 m/s, recorded at every time step and averaged over 10^4 steps before plotting the force-displacement curves.

5.3 Generation of DEM particle film models

Nanoparticle aggregates are built from primary particles following a discretized log-normal distribution, as measured from TEM image analyses [14]. The primary particle diameter ranges from 3 to 23 nm, with a stepsize of 1 nm (median

9.0 nm, $\sigma_G = 1.45$). These primary particles are combined using a Sequential Algorithm (SA) combined with a Cluster-Cluster Aggregation (CCA) as presented in Ref. [60]. This procedure generates random aggregates that follow the fractal distribution $N_p = k_f \cdot \left(\frac{d_g}{\bar{d}_s}\right)^{D_f}$, which is frequently used to describe FSP-synthesized particles [49,61–63]. Here, the amount of particles N_p in an aggregate is predicted using the diameter of gyration d_g, the Sauter diameter $\bar{d}_s$ (defined as $\bar{d}_s = 6V_{p,tot}/A_{p,tot}$, with $V_{p,tot}$ the total particle volume and $A_{p,tot}$ the total surface area), as well as the fractal prefactor k_f and the fractal dimension D_f. k_f and D_f are 1.0 and 1.8, respectively, for FSP-synthesized particles [61]. The aggregate generation algorithm combines 6 particles to one cluster using the SA. Subsequently, these clusters are combined using the CCA. The number distribution of rigid particle aggregates is estimated from Disc Centrifuge experiments [14]. The equation $N_p = k_m \cdot \left(\frac{d_m}{\bar{d}_s}\right)^{D_{fm}}$ is used according to [49]. In this equation d_m describes the mobility diameter from Disc Centrifuge experiments and k_m and D_{fm} are the mass mobility prefactor and dimension, respectively, that are 1.0 and 2.15 for FSP-synthesized particles. The number distribution ranges from 1 to 128 primary particles with a median of 36 particles and an arithmetic standard deviation σ_s of 0.5. The rigid aggregates are deposited individually on the bottom surface of a tetragonal simulation box according to diffusion and a thermophoretic velocity as discribed elsewhere [47]. The contact of the aggregate with the bottom surface or a previously deposited aggregate marks it as deposited. A deposited aggregate remains static during the ongoing film formation. The coefficient of diffusion for polydispersed nanoparticle aggregates is calculated according to Zhang et al. [64]. The program *zeno* is used to determine the hydrodynamic radius [65] and 56 angles are used to calculate the mean projected area PA of the deposited agglomerates. The friction factor f follows:

$$f = \frac{6\pi\mu R_H}{C_C\left(\frac{\lambda\pi R_H}{PA}\right)} \tag{14}$$

with the fluid viscosity μ, mean free path λ, the hydrodynamic radius R_H and the Cunningham slip correction C_C. The application of a thermophoretic velocity of 0.1 m/s [48] results in a film with a porosity of 98 %, which matches very well the typical experimental value [47,48]. The box presents a side length of $140\,\bar{d}_s$, which corresponds to a box with geometric sizes of $1.5814 \times 1.5814 \times 3.3580\ \mu m^3$.

5.4 DEM simulations

All DEM simulations are performed using the LIGGGHTS package [66], in which we have implemented the here-developed contact model, using a timestep $\Delta t = 0.5$ ps. Capillary forces and solvation forces are implemented using a tabulated potential to reduce computational cost. Initial relaxation of each simulated system is performed using a viscosity term acting on all particles (viscosity of 10 pN/(ms^{-1})). The action of this 'environmental viscosity', together with the friction terms in the contact model, guarantees that the systems evolve quasi-statically, with sufficient dissipation of the kinetic energy that builds up as a consequence of the nanoparticle rearrangements under mechanical stress. The AFM tip with a side length of 0.8 μm, represented by non-interacting and rigid primary particles with 20 nm radius, is placed above the film without any initial contact to the film. The dynamical simulations are then carried out in the micro-canonical ensemble, with the sole energy dissipation of the DEM contact model able to maintain the system under quasi-static conditions. The tip is moved with a constant velocity of −0.5 m/s along the z direction and the forces acting on the tip particles are averaged over periods of 10 ns, equaling a tip displacement of 5 nm. After reaching a repulsive force of 2 nN, the tip velocity is slowly decreased, reversed and then again increased to +0.5m/s within a period of 0.2 μs. Periodic boundary conditions are applied to the simulation box, with the bottom layer of aggregates kept fixed in order to mimic an underlying sample holder.

References

1. Zhu, H.P., Zhou, Z.Y., Yang, R.Y., Yu, A.B.: Discrete particle simulation of particulate systems: a review of major applications and findings. Chem. Eng. Sci. **63**(23), 5728–5770 (2008)
2. Min, Y., Akbulut, M., Kristiansen, K., Golan, Y., Israelachvili, J.: The role of interparticle and external forces in nanoparticle assembly. Nat. Mater. **7**(7), 527–538 (2008)
3. Cundall, P.A., Strack, O.D.L.: A discrete numerical model for granular assemblies. Geotechnique **29**(1), 47–65 (1979)
4. Zhu, H.P., Zhou, Z.Y., Yang, R.Y., Yu, A.B.: Discrete particle simulation of particulate systems: theoretical developments. Chem. Eng. Sci. **62**(13), 3378–3396 (2007)
5. Schilde, C., Burmeister, C.-F., Kwade, A.: Measurement and simulation of micromechanical properties of nanostructured aggregates via nanoindentation and DEM-simulation. Powder Technol. **259**, 1–13 (2014)
6. Chandler, M.Q., Peters, J.F., Pelessone, D.: Discrete element modeling of calcium-silicate-hydrate. Model. Simul. Mater. Sci. **21**(5), 055010 (2013)
7. Boltachev, G.S., Lukyashin, K.E., Shitov, V.A., Volkov, N.B.: Three-dimensional simulations of nanopowder compaction processes by granular dynamics method. Phys. Rev. E **88**(1), 012209 (2013)
8. Moreno-Atanasio, R., Antony, S.J., Williams, R.A.: Influence of interparticle interactions on the kinetics of self-assembly and mechanical strength of nanoparticulate aggregates. Particuology **7**(2), 106–113 (2009)
9. Luding, S.: Cohesive, frictional powders: contact models for tension. Granul. Matter **10**(4), 235–246 (2008)
10. Laube, J., Salameh, S., Kappl, M., Mädler, L., Colombi Ciacchi, L.: Contact forces between TiO_2 nanoparticles governed by an

interplay of adsorbed water layers and roughness. Langmuir **31**, 11288–11295 (2015)
11. Laube, J., Dörmann, M., Schmid, H.-J., Mädler, L., Colombi Ciacchi, L.: Dependencies of the adhesion forces between TiO_2 nanoparticles on size and ambient humidity. J. Phys. Chem. C **121**, 15294–15303 (2017)
12. Salameh, S., Schneider, J., Laube, J., Alessandrini, A., Facci, P., Seo, J.W., Colombi Ciacchi, L., Mädler, L.: Adhesion mechanisms of the contact interface of TiO_2 nanoparticles in films and aggregates. Langmuir **28**(31), 11457–11464 (2012)
13. Mädler, L., Kammler, H.K., Mueller, R., Pratsinis, S.E.: Controlled synthesis of nanostructured particles by flame spray pyrolysis. J. Aerosol Sci. **33**, 369–389 (2002)
14. Salameh, S., Scholz, R., Seo, J.W., Mädler, L.: Contact behavior of size fractionated TiO_2 nanoparticle agglomerates and aggregates. Powder Technol. **256**, 345–351 (2014)
15. Fabre, A., Salameh, S., Colombi Ciacchi, L., Kreutzier, M., Ommen, J.R.: Contact mechanics of highly porous oxide nanoparticle agglomerates. J. Nanopart. Res. **18**, 200 (2016)
16. Salameh, S., Veen, M.A., Kappl, M., Ommen, J.R.: Contact forces between single metal oxide nanoparticles in gas-phase applications and processes. Langmuir **33**, 2477–2484 (2017)
17. Krylov, S.Y., Frenken, J.W.M.: The physics of atomic-scale friction: basic considerations and open questions. Phys. Status Solidi B **251**(4), 711–736 (2014)
18. Dong, Y., Perez, D., Voter, A.F., Martini, A.: The roles of statics and dynamics in determining transitions between atomic friction regimes. Tribol. Lett. **42**(1), 99–107 (2011)
19. Gao, J., Luedtke, W.D., Gourdon, D., Ruths, M., Israelachvili, J.N., Landman, U.: Frictional forces and amontons' law: from the molecular to the macroscopic scale. J. Phys. Chem. B **108**(11), 3410–3425 (2004)
20. Park, J.Y., Salmeron, M.: Fundamental aspects of energy dissipation in friction. Chem. Rev. **114**(1), 677–711 (2014)
21. Szlufarska, I., Chandross, M., Carpick, R.W.: Recent advances in single-asperity nanotribology. J. Phys. D **41**(12), 123001 (2008)
22. Mo, Y., Turner, K.T., Szlufarska, I.: Friction laws at the nanoscale. Nature **457**(7233), 1116–1119 (2009)
23. Luan, B., Robbins, M.O.: The breakdown of continuum models for mechanical contacts. Nature **435**(7044), 929–932 (2005)
24. Jinesh, K., Frenken, J.: Experimental evidence for ice formation at room temperature. Phys. Rev. Lett. **101**(3), 036101 (2008)
25. Israelachvili, J.N.: Intermolecular and Surface Forces. Elsevier, Oxford (2011)
26. Hertz, H.: Über die Berührung fester elastischer Körper. J. für die reine und Angew. Math. **92**, 156–171 (1882)
27. Isaak, D.G., Carnes, J.D., Anderson, O.L., Cynn, H., Hake, E.: Elasticity of TiO_2 rutile to 1800 k. Phys. Chem. Miner. **26**(1), 31–43 (1998)
28. Feistel, R.: A new equation of state for H_2O ice I_h. J. Phys. Chem. Ref. Data **35**(2), 1021 (2006)
29. Prandtl, L.: Ein Gedankenmodell zur kinetischen Theorie der festen Körper. Z. Angew. Math. Mech. **8**(2), 85–106 (1928)
30. Li, Q., Dong, Y., Perez, D., Martini, A., Carpick, R.W.: Speed dependence of atomic stick-slip friction in optimally matched experiments and molecular dynamics simulations. Phys. Rev. Lett. **106**(12), 126101 (2011)
31. Sang, Y., Dubé, M., Grant, M.: Dependence of friction on roughness, velocity, and temperature. Phys. Rev. E **77**(3), 036123 (2008)
32. Chandross, M., Webb, E., Stevens, M., Grest, G., Garofalini, S.: Systematic study of the effect of disorder on nanotribology of self-assembled monolayers. Phys. Rev. Lett. **93**(16), 166103 (2004)
33. Carpick, R.W., Agraït, N., Ogletree, D.F., Salmeron, M.: Variation of the interfacial shear strength and adhesion of a nanometer-sized contact. Langmuir **12**(13), 3334–3340 (1996)
34. Socoliuc, A., Bennewitz, R., Gnecco, E., Meyer, E.: Transition from stick-slip to continuous sliding in atomic friction: entering a new regime of ultralow friction. Phys. Rev. Lett. **92**(13), 134301 (2004)
35. Glosli, J., McClelland, G.: Molecular dynamics study of sliding friction of ordered organic monolayers. Phys. Rev. Lett. **70**(13), 1960–1963 (1993)
36. Friddle, R.W., Noy, A., De Yoreo, J.J.: Interpreting the widespread nonlinear force spectra of intermolecular bonds. Proc. Natl. Acad. Sci. **109**(34), 13573–13578 (2012)
37. Wenning, L., Müser, M.H.: Friction laws for elastic nanoscale contacts. Europhys. Lett. **54**(5), 693–699 (2001)
38. Carpick, R.W., Ogletree, D.F., Salmeron, M.: Lateral stiffness: a new nanomechanical measurement for the determination of shear strengths with friction force microscopy. Appl. Phys. Lett. **70**(12), 1548 (1997)
39. Enachescu, M., Oetelaar, R.J.A., Carpick, R.W., Ogletree, D.F., Flipse, C.F.J., Salmeron, M.: Atomic force microscopy study of an ideally hard contact: the diamond(111)/tungsten carbide interface. Phys. Rev. Lett. **81**(9), 1877–1880 (1998)
40. Ecke, S., Butt, H.-J.: Friction between individual microcontacts. J. Colloid Interf. Sci. **244**(2), 432–435 (2001)
41. Mindlin, R.D., Deresiewicz, H.: Elastic spheres in contact under varying oblique forces. J. Appl. Mech. Trans. ASME **20**(3), 327–344 (1953)
42. Zhou, Y.C., Wright, B.D., Yang, R.Y., Xu, B.H., Yu, A.B.: Rolling friction in the dynamic simulation of sandpile formation. Physica A **269**(2–4), 536–553 (1999)
43. Ai, J., Chen, J.-F., Rotter, J.M., Ooi, J.Y.: Assessment of rolling resistance models in discrete element simulations. Powder Technol. **206**(3), 269–282 (2011)
44. O' Sullivan, C., Bray, J.D.: Selecting a suitable time step for discrete element simulations that use the central difference time integration scheme. Eng. Comput. **21**(2/3/4), 278–303 (2004)
45. Meißner, R.H., Wei, G., Colombi Ciacchi, L.: Estimation of the free energy of adsorption of a polypeptide on amorphous SiO_2 from molecular dynamics simulations and force spectroscopy experiments. Soft Matter **11**, 6254–6265 (2015)
46. Melnikov, K., Mani, R., Wittel, F.K., Thielmann, M., Herrmann, H.J.: Models, algorithms and validation for opensource DEM and CFD–DEM. Phys. Rev. E **92**, 022206 (2015)
47. Mädler, L., Lall, A.A., Friedlander, S.K.: One-step aerosol synthesis of nanoparticle agglomerate films: simulation of film porosity and thickness. Nanotechnology **17**(19), 4783–4795 (2006)
48. Mädler, L., Roessler, A., Pratsinis, S.E., Sahm, T., Gurlo, A., Barsan, N., Weimar, U.: Direct formation of highly porous gas-sensing films by in situ thermophoretic deposition of flame-made Pt/SnO_2 nanoparticles. Sensors Actuators B Chem. **114**(1), 283–295 (2006)
49. Eggersdorfer, M.L., Gröhn, A.J., Sorensen, C.M., McMurry, P.H., Pratsinis, S.E.: Mass-mobility characterization of flame-made ZrO_2 aerosols: primary particle diameter and extent of aggregation. J. Colloid Interface Sci. **387**(1), 12–23 (2012)
50. Weber, A.P., Friedlander, S.K.: In situ determination of the activation energy for restructuring of nanometer aerosol agglomerates. J. Aerosol Sci. **28**(2), 179–192 (1997)
51. Mandzy, N., Grulke, E., Druffel, T.: Breakage of TiO_2 agglomerates in electrostatically stabilized aqueous dispersions. Powder Technol. **160**(2), 121–126 (2005)
52. Buesser, B., Gröhn, A.J., Pratsinis, S.E.: Sintering rate and mechanism of TiO_2 nanoparticles by molecular dynamics. J. Phys. Chem. C **115**(22), 11030–11035 (2011)
53. Schneider, J., Colombi Ciacchi, L.: First principles and classical modeling of the oxidized titanium (0001) surface. Surf. Sci. **604**(13–14), 1105–1115 (2010)

54. Schneider, J., Colombi Ciacchi, L.: A classical potential to model the adsorption of biological molecules on oxidized titanium surfaces. J. Chem. Theory Comput. **7**(2), 473–484 (2011)
55. Schopf, S.O., Salameh, S., Mädler, L.: Transfer of highly porous nanoparticle layers to various substrates through mechanical compression. Nanoscale **5**, 3764–3772 (2013)
56. Thakur, S.C., Morrissey, J.P., Sun, J., Chen, J.F., Ooi, J.Y.: Micromechanical analysis of cohesive granular materials using the discrete element method with an adhesive elasto-plastic contact model. Granul. Matter **16**, 383–400 (2014)
57. Hutter, J.L., Bechhoefer, J.: Calibration of atomic-force microscope tips. Rev. Sci. Instrum. **64**(11), 1868–1873 (1993)
58. Jorgensen, W.L., Chandrasekhar, J., Madura, J.D., Impey, R.W., Klein, M.L.: Comparison of simple potential functions for simulating liquid water. J. Chem. Phys. **79**(2), 926 (1983)
59. Plimpton, S.: Fast parallel algorithms for short-range molecular dynamics. J. Comput. Phys. **117**(1), 1–19 (1995)
60. Filippov, A.V., Zurita, M., Rosner, D.E.: Fractal-like aggregates: relation between morphology and physical properties. J. Colloid Interface Sci. **229**(1), 261–273 (2000)
61. Friedlander, S.K.: Smoke, Dust and Haze: Fundamentals of Aerosol Behavior. Wiley, New York (1977)
62. Ommen, J.R., Valverde, J.M., Pfeffer, R.: Fluidization of nanopowders: a review. J. Nanopart. Res. **3**, 1–29 (2012)
63. Eggersdorfer, M.L., Pratsinis, S.E.: The structure of agglomerates consisting of polydisperse particles. Aerosol Sci. Technol. **3**, 347–353 (2012)
64. Zhang, C., Thajudeen, T., Larriba, C., Schwartzentruber, T.E., Hogan, C.J.: Determination of the scalar friction factor for non-spherical particles and aggregates across the entire knudsen number range by direct simulation Monte Carlo (DSMC). Aerosol Sci. Technol. **46**(10), 1065–1078 (2012)
65. Mansfield, M.L., Douglas, J.F., Garboczi, E.J.: Intrinsic viscosity and the electrical polarizability of arbitrarily shaped objects. Phys. Rev. E **64**(6), 061401 (2001)
66. Kloss, C., Goniva, C., Hager, A., Amberger, S., Pirker, S.: Models, algorithms and validation for opensource DEM and CFD–DEM. Prog. Comput. Fluid Dyn. **12**(2/3), 140 (2012)